

ORIGINAL ARTICLE

Ventricular Function

Three-Dimensional Myocardial Strains at End-Systole and During Diastole in the Left Ventricle of Normal Humans

Joost P. A. Kuijjer,^{1,*} J. Tim Marcus,¹ Marco J. W. Götte,²
Albert C. van Rossum,² and Robert M. Heethaar¹

¹Department of Clinical Physics and Informatics and ²Department of Cardiology, Institute for Cardiovascular Research ICaR-VU, Vrije Universiteit, Amsterdam, The Netherlands

ABSTRACT

This paper presents the three-dimensional strains in the normal human left ventricle (LV) at end-systole and during diastole. Magnetic resonance tissue tagging was used to measure strain in the left-ventricular heart wall in 10 healthy volunteers aged between 28 and 61 years. The three-dimensional motion was calculated from the displacement of marker points in short- and long-axis cine images, with a time resolution of 30 msec. Homogeneous strain analysis of small tetrahedrons was used to calculate deformation in 18 regions of the LV over a time span of 300 msec starting at end systole. End-systolic radial strain was largest near the heart base, and circumferential and longitudinal strains were largest near the apex. During diastole, the circumferential–longitudinal shear strain (associated with LV torsion) was found to recover earlier than the axial strains. Assessment of three-dimensional diastolic strain is possible with MR tagging. Comparison of patient strain against normal strain may permit early detection of regional diastolic dysfunction.

Key Words: *Magnetic resonance tagging; Left ventricle; Left-ventricular function; Diastole; Strain analysis*

*Corresponding author. Mail address: P.O. Box 7057, 1007 MB Amsterdam, The Netherlands. Fax: +31-20-4444147; E-mail: jpa.kuijjer@vumc.nl

INTRODUCTION

Diastolic heart failure^[1,2] is a common clinical disorder. Although congestive heart failure is often associated with systolic dysfunction, as many as one-third of the patients with signs of congestive heart failure appear to have a normal systolic function, which implicates that impaired diastolic function is the primary cause of heart failure in these patients. Over the last two decades, much interest has been shown in the mechanisms of diastolic function, and its relation with systolic function. Particularly, it has been shown that abnormalities in diastolic function may precede systolic dysfunction in patients with arterial hypertension^[3] and aortic stenosis.^[4] Abnormal diastolic filling has been reported in patients with coronary artery disease and normal systolic function.^[5] The left ventricular (LV) filling pattern assessed very early after myocardial infarction can identify patients at risk of acute heart failure and cardiac death in the first year after infarction.^[6]

The systolic torsion (twisting or wringing motion) of the left ventricle (LV) and the subsequent untwisting during diastole appears to play a crucial role in diastolic filling. It has been speculated that early untwisting during isovolumetric relaxation is essential to create a rapid pressure fall in the LV,^[7] a prerequisite for fast and early diastolic filling. Indeed, investigators have recently demonstrated delayed untwisting in pressure-overloaded hearts.^[8] While Rademakers et al.^[7] already observed increased torsion and more rapid untwisting in dobutamine-stimulated hearts, Dong and co-workers^[9] have now shown that the volume-torsion relation may provide a load-independent measure of contractility.

Magnetic resonance imaging (MRI) with myocardial tissue tagging^[10,11] has been proven a powerful tool for noninvasive quantification of three-dimensional (3D) LV systolic deformation or strain in normal and pathological subjects.^[12–18] With MR tagging, the magnetization of tissue is locally saturated, as to create markers in the tissue. The tissue with altered magnetization appears darker in MR images compared with the unaltered tissue. Usually, the magnetization is saturated in a series of tissue slices orthogonal to the image plane, to create a set of parallel dark lines or a dark grid in the image. As the tissue moves and deforms during the cardiac cycle, the motion of the tagged lines or grid reflects the underlying motion of the imaged tissue. Post-processing allows quantification of the 2D motion as a function of time. By combining data from short-axis (SA) and long-axis

tagged images, the 3D deformation of the LV heart wall can be calculated.

Human 3D strains measured with MR tagging have been reported during systole,^[18] at end-systole (ES)^[13] and during isovolumic relaxation,^[19] Also, the LV torsion has been quantified at ES^[20] and more recently during diastole as well.^[4] In this paper we present the LV 3D strains at ES and evolution of strain during the first 300 msec of diastole, measured in healthy volunteers.

METHODS

Ten healthy male volunteers (28–61 years) were subjected to MR imaging. The volunteers had no prior history of cardiovascular disease. The electrocardiograms of all volunteers showed sinus rhythm without pathology. Table 1 lists data of the individual subjects. The scan protocol was approved by the medical ethical committee of our hospital, and all subjects gave informed consent. The ES strains of five volunteers have been used in the group average of a previous publication.^[21] Nine subjects were imaged on a Magnetom Vision 1.5 Tesla scanner, one subject was imaged on a Magnetom Impact 1.0 Tesla scanner (Siemens, Erlangen, Germany).

Cine Imaging Protocol and Analysis

In order to assess the basic parameters of LV function listed in Table 1, the volunteers were subjected to MR cine imaging. A detailed description of this protocol is given by Marcus et al.^[22] In short, a series of SA image planes was defined starting at the base of the LV, encompassing the entire LV from base to apex. At every SA plane, a series of images was acquired in a single breathhold using a gradient echo cine sequence with segmented *k*-space yielding a temporal resolution of 40 msec.

The images were processed using a dedicated software package (MASS Dept. of Radiology, Leiden University Medical Center, Leiden, The Netherlands). End-diastole (ED) was defined as the first temporal frame directly after the R-wave of the ECG. Epi- and endocardial contours were manually traced, and the papillary muscles were excluded from the LV volume. End-diastolic volume (EDV), end-systolic volume (ESV), and ejection fraction (EF) were calculated from these contours. Cardiac output (CO) was calculated from the listed heart rate and volumes. The filling rate was calculated from the time course of the volume of the LV cavity during diastole. The peak-filling rate (PFR) is

Table 1
Healthy Volunteer Data

Subject ^a	Age (Years)	Heart Rate (bpm) ^b	Weight (kg)	EDV (mL) ^c	ESV (mL) ^c	EF (%) ^c	CO (L min ⁻¹) ^c	PFR (mL s ⁻¹) ^c
1	50	52	88	118	29	76	4.7	392
2	58	44	90	147	36	76	4.9	379
3	52	68	71	99	28	72	4.8	373
4	44	75	99	137	44	68	7.0	382
5	49	74	97	110	40	64	5.2	360
6	61	55	84	150	60	60	5.0	349
7	51	61	78	139	55	60	5.1	297
8	35	59	81	146	70	52	4.5	342
9	31	70	80	120	45	62	5.2	320
10	28	59	74	129	46	65	4.9	395
Mean ± SD	46 ± 11	62 ± 10	84 ± 9	130 ± 17	45 ± 13	65 ± 8	5.1 ± 0.7	359 ± 32

^aAll subjects white male.

^bAverage heart rate during MR investigation.

^cCalculated from short-axis cine MRI.

defined as the maximum slope of this time course. The PFR gives some indication of LV diastolic function, and is therefore listed in Table 1.

Tag Imaging Protocol

For the tagged images, we applied a 2D tagging grid during the first 20 msec after the ECG R-wave. Two series of five nonselective radio-frequency pulses of 14, 33, 49, 33, and 14° separated by magnetic field gradients produced spatial modulation of magnetization (SPAMM).^[11] The grid line distance was 7 mm. A gradient-echo cine imaging sequence (24–30 frames, temporal resolution 30 msec) was applied for systolic and diastolic imaging. The following parameter settings were used: 15° excitation angle, 3.8/4.8 msec (Impact/Vision) echo time, 10 msec repetition time, segmented k -space with 3 k_y -lines per heart beat, 144 × 256 matrix, 250 × 250 mm² field of view and 6 mm slice thickness.

Firstly, a stack of five to seven SA slices was imaged. The image planes were planned orthogonal to the long axis (LA) of the LV. The slice distance was 10 mm. This was followed by a series of three LA images. The LA image planes were orthogonal to the SA image planes and radially distributed around the LV LA. The angular spacing between the LA image planes was 60°. The first LA image plane was set parallel to the inter-ventricular septum. The field of view was enlarged to 300 × 300 mm² for the LA images.

To avoid breathing motion artifacts, we employed a multiple brief breath hold scheme.^[23] Image data was acquired only during one cardiac cycle at end exhalation, thus approximating a constant heart position throughout the acquisition. The subject is then given about five or six seconds to in- and exhale before acquisition of the next set of three k_y -lines. In total, 48 of these brief expiration breath holds are required for the acquisition of 144 k_y -lines, leading to an imaging time between 5 and 6 min per image plane. A secondary advantage of this scheme is that the heart rate, which varies substantially during the breathing cycle or during a long breath hold, is relatively constant during acquisition in short breath holds. The heart rate during acquisition is listed in Table 1. Figure 1 shows three selected frames of a mid-ventricular and an apical SA slice, and of LA slice parallel to the septum.

Analysis of Tagged Images

Contours, which outline the LV endo- and epicardial borders, and tag line intersections (tag points) were tracked semi-automatically using “snakes” with Spammvu (Univ. of Pennsylvania, Philadelphia, PA).^[24] The tracked tag points were checked and edited manually when necessary. The time required for semi-automatic tracking of all acquired time frames in eight image planes of one subject, and manual editing of ten time frames from end systole onwards was about 5 hr. Manual editing was the most time-consuming part.

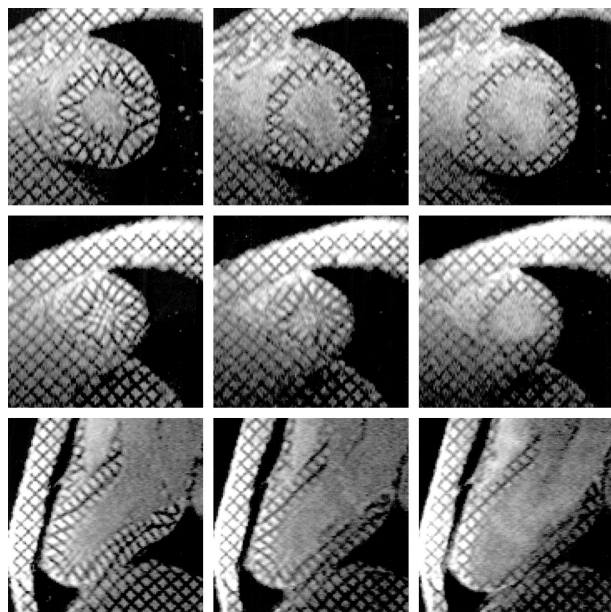


Figure 1. Three selected time frames of a tagged MR cine with a time resolution of 30 msec. Top row: mid-ventricular slice, mid row: apical slice, bottom row: long-axis slices parallel to the septum. The first column shows the cine frame at ES (frame 11, $t = 300$ msec), when deformation was maximal for this subject. The second column is frame 16 at $t = 450$ msec (ES + 150 msec), when blurring due to motion from rapid filling was maximal on the LA image (bottom). The third column is frame 20 at $t = 570$ msec (ES + 270 msec), which was the last time frame analyzed for this subject.

The ES image was defined as the image that shows the smallest LV cavity, just before a reversal of the wall motion was observed. The ES time frames and the nine following diastolic time frames were selected for strain calculation. Thus, the time span for strain calculations was between $t = \text{ES}$ and $t = \text{ES} + 270$ msec.

Three-Dimensional Displacement and Strain

The tracked tag points were used to calculate 3D displacement vectors using a one-dimensional displacement field fit. Firstly, the geometry of a finite element (FE) model^[25] was fitted to the tracked LV contours on the SA and LA tagged cines between ES and ES + 270 msec. Next, the 1D displacement field was fitted to the longitudinal motion measured in the LA images. Details of this method have been described previously.^[21] The fitted longitudinal displacement field was used to calculate the through-plane displacement at the locations of the SA tag points. By this procedure, the 3D

displacement of the material points imaged as a SA tag point in the deformed state was fully known: the SA in-plane motion was calculated directly from the SA tag points, while the through-plane motion was calculated using the FE displacement field. End diastole was defined as the reference state (undeformed state) for all displacements. The displacement vectors were calculated for each of the 10 time frames separately.

For the purpose of homogeneous strain analysis, the tracked material points were connected into a mesh of small tetrahedrons ($\sim 0.1 \text{ cm}^3$). Figure 2 shows an example of the geometry of the tetrahedrons in one subject. The size of the tetrahedrons depends on the grid size (7 mm) and on the slice distance (10 mm).

With homogeneous strain analysis, it is assumed that the strain within each tetrahedron is constant. The deformation gradient tensor \mathbf{F} was calculated for each tetrahedron, similar to the 2D analysis described by Axel et al.^[26] The Lagrangian strain tensor was then defined by:

$$\mathbf{E} = \frac{1}{2}(\mathbf{F}^T \mathbf{F} - \mathbf{1}) \quad (1)$$

The reference state (undeformed state) for the strain calculation was always ED.

The strain tensor was evaluated in local cardiac coordinates. For this reason, we required the ED geometry of the LV. An additional FE geometry was fitted to the LV contours in the last frame of the cine (approximately 750 msec after ED). Although the late-diastolic geometry is not exactly equal to the ED geometry, we have opted for this geometry because the LV blood pool is inseparable from the myocardium on the first image of the tagging cine.

A local coordinate system was defined using the curved surface equidistant between the fitted endo- and epicardial surface. The radial unit base vector \mathbf{e}_r was defined outward and normal to this surface, as shown in Fig. 2c. The circumferential base vector \mathbf{e}_c was defined orthogonal to both \mathbf{e}_r and the LV LA. Viewed from the LV base, \mathbf{e}_c points counter-clockwise. The longitudinal base vector was defined parallel to the centered surface by the cross-product $\mathbf{e}_l = \mathbf{e}_r \times \mathbf{e}_c$. The direction of this vector is from apex to base.

The strain tensor \mathbf{E} was transformed into the rcl-coordinate system. Most previous studies, such as those by Young et al.^[13] and Moore et al.,^[18] have reported the six independent components of \mathbf{E} . In this study, we chose to express the axial strains (also referred to as normal strains) as a relative change of length, and to express the

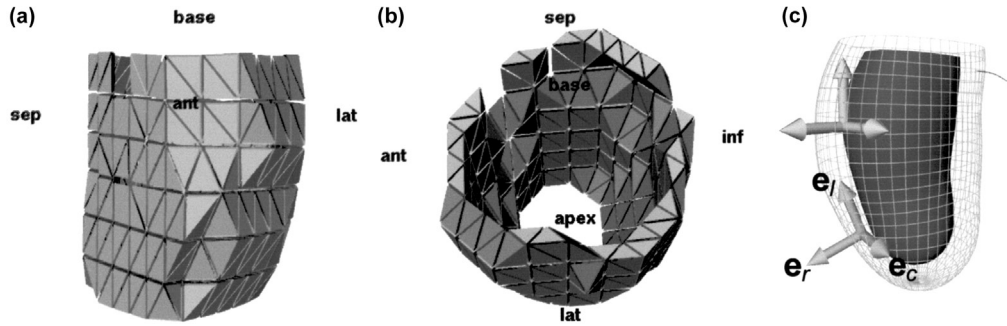


Figure 2. Example of the end-diastolic geometry of the tetrahedrons used for homogeneous strain analysis of the LV heart wall in one of the subjects. The left panel (a) is a side view onto the anterior free wall. The middle panel (b) gives a top view, looking from base to apex onto the LV cavity. The labels give the orientation of the LV: “sep” for septum, “ant” for anterior, “lat” for lateral and “inf” for inferior. The height of the tetrahedrons is approximately 10 mm, the length of the short sides of the top (or bottom) of the tetrahedrons is approximately 7 mm. The myocardial volume encompassed by each tetrahedron is about 0.1 cm³. (c) shows an example of the ED geometry and the local cardiac coordinates used for strain analysis in one of the subjects. The dark gray surface was fitted to the SA and LA endocardial contours. The wire-frame surface was fitted to the epicardial contours. The mid-wall surface (not shown in the figure), which is equidistant to the endo- and epicardial surfaces, defined the local radial, circumferential, and longitudinal directions. The base vectors e_r , e_c , and e_l are visualized at two locations in the heart wall; they follow the curvature of the mid-wall surface.

shear strain as a change in angle:^[27]

$$\begin{aligned} \epsilon_i &= \sqrt{1 + 2E_{ii}} - 1; \\ \sin \alpha_{ij} &= \frac{2E_{ij}}{(\epsilon_i + 1)(\epsilon_j + 1)} \end{aligned} \quad (2)$$

where E_{ii} are diagonal elements and E_{ij} are off-diagonal elements of \mathbf{E} (i and j index the direction, and are replaced by either r, c, or l). The interpretation of the value of the axial strain ϵ and shear angle α is more intuitive than the components of \mathbf{E} : suppose we focus on a small cube of myocardium with sides aligned with the rcl-directions (see sketch in Fig. 3). For example, ϵ_c gives the relative change in length of the circumferential edge of the cube (l_c in Fig. 3). A value of $\epsilon_c = l'_c/l_c - 1 = -0.20$ means that the cube of myocardium has shortened 20% in the circumferential direction. The shear angles can be interpreted as the change in angle between two initially orthogonal edge segments. For example, α_{cl} gives the change in angle between the circumferential and longitudinal edge segments (see Fig. 3). This shear angle may be interpreted as the local contribution to global torsion. Note that the results of our study are easily compared with studies reporting the components of \mathbf{E} by using Eq. (2).

The heart was divided into three longitudinal levels and six circumferential segments using the ED geometry.

The longitudinal levels were defined by dividing the heart wall between base and apex into three equally sized parts. The circumferential segments were all 60° in size. The average strain within a segment was calculated by averaging over all tetrahedrons within a segment. Variation in ES strain between longitudinal levels or circumferential segments was tested by repeated measures analysis of variance. Bonferroni correction was applied to adjust for multiple comparisons. The significance level for statistical tests was 0.05.

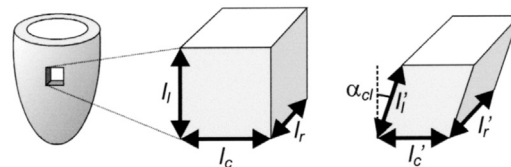


Figure 3. This sketch shows the intuitive interpretation of the axial strains ϵ and the shear angle α_{cl} . Suppose we focus on a small cube in the LV heart wall, with sides aligned with the radial, circumferential, and longitudinal directions. The ϵ_r gives the relative change in length of the radial edge segment during deformation: $\epsilon_r = l'_r/l_r - 1$. Similar interpretations hold for ϵ_c and ϵ_l . The shear angle α_{cl} gives the change in angle between the initially orthogonal circumferential and longitudinal line segments. For clarity, the two shear angles α_{rc} and α_{rl} are not shown in the sketch.

To compare the temporal evolution of the various strain parameters we normalized the global diastolic strains to the ES value of the strains: $\varepsilon_{\text{nor}}(t) = \varepsilon(t)/\varepsilon(\text{ES})$ where $\varepsilon(\text{ES})$ is the axial strain at ES. The normalized shear strain was defined by $\alpha_{\text{nor}}(t) = \alpha(t)/\alpha(\text{ES})$. The maximum normalized strain rate was calculated by taking maximum of the temporal derivative of the normalized strain: $\max(d\varepsilon_{\text{nor}}/dt)$. Effects of age on strain parameters were assessed by linear regression of the global average strain of all tetrahedrons in the subjects. Linear regression was performed at ES and at ES + 270 msec for ε_r , ε_c , ε_l , and α_{cl} , and for the maximum normalized strain rate. Statistical tests and regression

analysis were carried out with SPSS for Windows, release 9.0.1 (SPSS Inc., Chicago, IL).

RESULTS

End-Systolic Strains

End systole was established at 346 ± 19 msec (mean \pm standard deviation) after the R-wave. The average per segment of all six ES strain components is listed in Table 2. We first calculated the strain in a segment for each subject, followed by calculation of mean and SD between subjects. The second column

Table 2

Average End-Systolic Strains

Strain	Mean	Anterior	Antero-lateral	Postero-lateral	Inferior	Infero-septal	Antero-septal
ε_r							
Mean	0.31 ± 0.04	0.31 ± 0.05	0.33 ± 0.07	0.31 ± 0.07	0.28 ± 0.04	0.30 ± 0.03	0.30 ± 0.05
Base	0.34 ± 0.04	0.33 ± 0.06	0.42 ± 0.08	0.38 ± 0.09	0.30 ± 0.07	0.31 ± 0.04	0.32 ± 0.07
Mid	0.29 ± 0.04	0.29 ± 0.07	0.29 ± 0.07	0.28 ± 0.08	0.27 ± 0.04	0.31 ± 0.04	0.31 ± 0.06
Apex	0.28 ± 0.07	0.32 ± 0.09	0.27 ± 0.08	0.29 ± 0.12	0.26 ± 0.05	0.26 ± 0.04	0.27 ± 0.10
ε_c							
Mean	-0.21 ± 0.02	-0.23 ± 0.02	-0.23 ± 0.03	-0.22 ± 0.02	-0.18 ± 0.02	-0.20 ± 0.02	-0.21 ± 0.02
Base	-0.19 ± 0.01	-0.22 ± 0.02	-0.21 ± 0.03	-0.21 ± 0.03	-0.16 ± 0.02	-0.18 ± 0.01	-0.19 ± 0.02
Mid	-0.21 ± 0.02	-0.23 ± 0.02	-0.24 ± 0.03	-0.22 ± 0.03	-0.18 ± 0.02	-0.20 ± 0.03	-0.21 ± 0.02
Apex	-0.24 ± 0.01	-0.27 ± 0.02	-0.26 ± 0.02	-0.25 ± 0.03	-0.21 ± 0.04	-0.23 ± 0.02	-0.25 ± 0.02
ε_l							
Mean	-0.16 ± 0.02	-0.16 ± 0.02	-0.17 ± 0.02	-0.18 ± 0.02	-0.17 ± 0.02	-0.16 ± 0.01	-0.15 ± 0.02
Base	-0.17 ± 0.02	-0.15 ± 0.03	-0.19 ± 0.03	-0.20 ± 0.02	-0.19 ± 0.03	-0.14 ± 0.02	-0.13 ± 0.03
Mid	-0.16 ± 0.02	-0.15 ± 0.03	-0.16 ± 0.03	-0.17 ± 0.02	-0.15 ± 0.02	-0.15 ± 0.01	-0.15 ± 0.02
Apex	-0.18 ± 0.02	-0.18 ± 0.03	-0.18 ± 0.02	-0.18 ± 0.02	-0.19 ± 0.02	-0.19 ± 0.02	-0.20 ± 0.02
α_{rc} (deg)							
Mean	1.1 ± 1.2	4.6 ± 3.8	0.9 ± 2.7	0.2 ± 1.8	-0.5 ± 3.2	1.1 ± 2.6	1.4 ± 2.2
Base	-2.3 ± 1.8	-1.4 ± 4.2	-1.2 ± 4.0	-2.0 ± 2.6	-3.0 ± 3.8	-1.5 ± 1.9	-3.7 ± 3.9
Mid	2.0 ± 0.6	7.2 ± 3.0	1.0 ± 3.5	0.9 ± 2.1	0.0 ± 3.2	1.0 ± 2.8	2.6 ± 2.4
Apex	5.4 ± 1.2	9.5 ± 5.1	3.8 ± 4.0	4.5 ± 2.0	4.5 ± 4.4	4.9 ± 4.4	5.9 ± 2.5
α_{rl} (deg)							
Mean	0.6 ± 1.4	0.2 ± 3.3	3.1 ± 2.4	1.4 ± 1.8	0.6 ± 1.8	-1.8 ± 3.2	-0.3 ± 2.9
Base	-2.4 ± 3.3	-5.1 ± 4.5	0.0 ± 7.7	-2.5 ± 9.2	-2.0 ± 4.9	-4.6 ± 5.0	-2.0 ± 4.0
Mid	2.5 ± 2.3	1.7 ± 3.6	4.9 ± 5.6	3.6 ± 2.4	3.1 ± 2.7	0.3 ± 3.9	0.5 ± 3.8
Apex	2.1 ± 3.6	5.7 ± 6.7	4.3 ± 4.8	2.5 ± 4.1	0.0 ± 5.1	-0.4 ± 4.8	1.3 ± 3.7
α_{cl} (deg)							
Mean	7.3 ± 1.5	7.0 ± 1.8	8.0 ± 1.5	8.4 ± 1.7	7.0 ± 2.6	7.0 ± 1.5	5.9 ± 2.5
Base	7.3 ± 2.0	8.2 ± 2.6	9.9 ± 1.7	9.4 ± 3.5	5.8 ± 4.9	6.0 ± 2.5	5.7 ± 2.7
Mid	7.3 ± 1.4	6.5 ± 2.8	7.1 ± 1.7	8.7 ± 1.7	8.1 ± 2.3	7.1 ± 1.7	5.8 ± 3.1
Apex	7.0 ± 1.3	5.6 ± 2.4	6.8 ± 1.9	6.3 ± 3.1	8.0 ± 3.0	8.1 ± 1.5	7.2 ± 3.4

Data are mean \pm SD, calculated over $n = 10$ healthy volunteers. The "mean" column reports the strain at basal, mid, and apical levels without subdivision in circumferential segments. The "mean" rows report the strain in circumferential segments without subdivision in longitudinal levels. The overall mean and SD were calculated using the global mean strain of each subject.

(“mean”) lists the strain in the basal, mid, and apical levels prior to subdivision in circumferential segments. The radial strain was larger at the base than mid ($P < 0.05$) and apex ($P < 0.01$). The differences between longitudinal levels were all highly significant ($P < 0.001$); circumferential shortening was stronger at the apex than at the base. The longitudinal shortening was slightly larger at the apex than at the mid-level ($P < 0.001$). Both shear angles α_{rc} and α_{rl} were negative in all basal segments, and positive at the mid- and apical levels. Differences in α_{rc} between the longitudinal levels were all significant ($P < 0.001$). α_{rl} at the base was different from mid and apex ($P < 0.05$). Differences between longitudinal levels were not significant for α_{cl} .

All strains except ϵ_r showed significant variation between circumferential segments. The circumferential strain was stronger in both anterior and antero-lateral segments than in the inferior ($P < 0.001$) and infero-septal ($P < 0.01$) segments. The largest difference in longitudinal strain was between postero-lateral and antero-septal segments ($P < 0.001$). Shear strains also showed regional differences, the largest being anterior

vs. inferior ($P < 0.01$) for α_{rc} , antero-lateral vs. infero-septal ($P < 0.01$) for α_{rl} , and postero-lateral vs. antero-septal ($P < 0.05$) for α_{cl} .

Diastolic Strain Evolution

The segment-wise results of the diastolic strain are shown in Fig. 4. The reference state (undeformed state, with zero strain indicated by the dotted line) was ED for all strains. The covered time-span runs from ES to 270 msec into diastole; the time axis is relative to $t = ES$. The solid line is the mean strain in a segment, the error bars indicate $\pm 2SD$. The mean and SD at $t = ES$ are identical to those in Table 2. The results of ϵ_c and ϵ_l had the least variability of all six strain parameters, as indicated by the small error bars. A monotonic relaxation of axial strains was observed in most of the segments. The antero-lateral and postero-lateral segments tended to show a delayed relaxation of ϵ_c and ϵ_l compared with the other segments.

The shear strains α_{rc} and α_{rl} did not reveal a clear pattern: variability between subjects and between

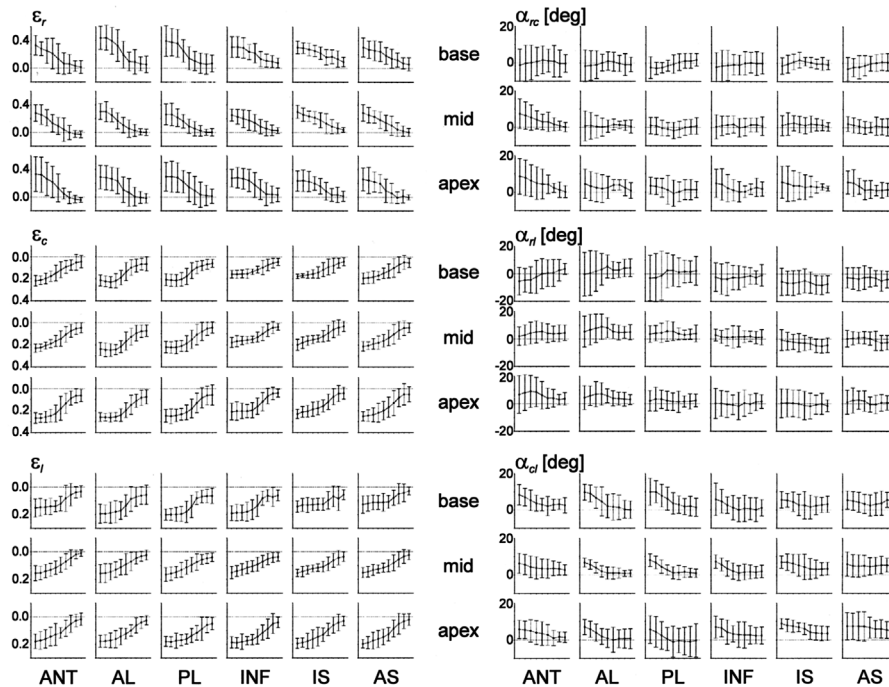


Figure 4. Temporal evolution per segment of six strain parameters during diastole averaged over all subjects. The time coverage of each plot is from ES to ES + 270 msec. Each point corresponds to the strain in a segment in one time frame, with the error bars specifying ± 2 SD. The time interval between two points is 30 msec. The undeformed state was ED in all time frames, therefore, the ED strain is zero by definition, which is indicated by the dotted line. The circumferential segments are labeled by their abbreviations: ANT = anterior, AL = antero-lateral, PL = postero-lateral, INF = inferior, IS = infero-septal, and AS = antero-septal.

segments was large. In the mid-infero-septal segment, we even observed an *increase* in magnitude of α_{r1} (paired t -test, $t = \text{ES}$ vs. $t = \text{ES} + 270$ msec, $P < 0.005$). The mid-diastolic strain at $t = \text{ES} + 270$ msec gives some indication of the strain evolution during late diastole. The global mid-diastolic cl-shear strain was $2.2 \pm 0.8^\circ$ ($P < 0.001$). The cl-shear in the infero-septal and antero-septal segments did not show a strong decay during early diastole.

To compare the temporal evolution of the three axial strains and α_{c1} we normalized these strains to their ES value. The shear strains α_{rc} and α_{r1} were not further analyzed because the global mean of these strains was small as a result of the regional differences. The plot of the normalized strains in time is given in Fig. 5. The 50% recovery time was defined as the time at which the normalized strain crossed the 0.5-level. The 50% recovery times are listed in Table 3. The time differences between the 50% recovery of α_{c1} and the axial strains are in the third column. The 50% recovery of α_{c1} occurs before 50% recovery of the axial strains, which is clearly shown in Fig. 5. This graph also shows that the recovery of radial strain is almost complete at $t = \text{ES} + 270$ msec (mid-diastole), whereas α_{c1} is only partially recovered at mid-diastole.

Table 4 gives the results of the mean peak strain rate. If the strain rate was positive, the maximum strain rate is listed. For negative strain rates, the minimum is listed. To

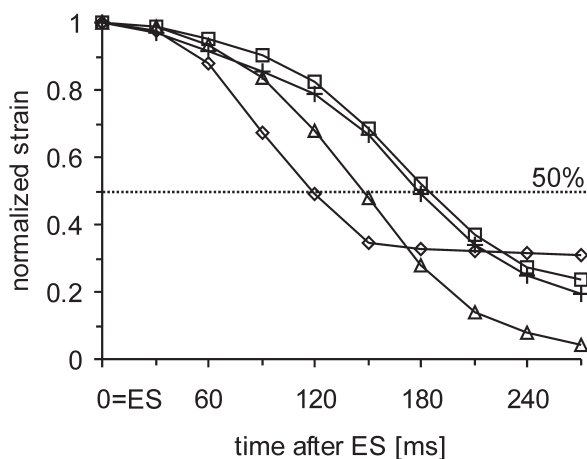


Figure 5. Normalized diastolic strain evolution averaged over all subjects. The ED strain is 0 and the ES strain is 1 by definition. This plot shows the relative timing of the recovery of the axial strains and the cl-shear strain. Symbol legend: $\Delta = \varepsilon_r$, $\square = \varepsilon_c$, $+$ = ε_l , $\diamond = \alpha_{c1}$. The dotted line indicates the 50% recovery line.

Table 3

Fifty Percent Recovery Time of Diastolic Strain

Strain	$t_{50\%}$ (ms)	$t_{50\%} - t_{50\%}(\alpha_{c1})$ (ms)
ε_r	147 ± 29	$26 \pm 25^*$
ε_c	184 ± 37	$62 \pm 25^{**}$
ε_l	179 ± 23	$57 \pm 29^{**}$
α_{c1}	122 ± 35	0

All values mean \pm SD.

* $P < 0.05$, ** $P < 0.001$ in paired t -test, $t_{50\%}$ vs. $t_{50\%}(\alpha_{c1})$.

facilitate comparison between the different strain parameters, we also report the peak strain rates normalized to ES strain. The peak normalized strain was larger (more negative) for the radial strain than for the circumferential strain ($P < 0.001$ in paired t -test).

DISCUSSION

It has been stated that the degree of uniformity of contraction and relaxation is an important determinant of diastolic function.^[1] This paper shows that MR-tagging and 3D strain analysis can be applied to evaluate regional ES and early diastolic deformation.

End-Systolic Strain

The results at ES in Table 2 may be compared to the results of Young et al.^[13] and Moore et al.^[18] Both papers report the values of the Lagrangian strain tensor \mathbf{E} , but these are easily converted to the parameters reported in this paper by using Eq. (2). The range of ε_r was 0.26–0.42 (mean 0.31), similar to the radial strains reported by Moore (range of ε_r : 0.30–0.52, mean 0.38, calculated

Table 4

Peak Diastolic Strain Rates

Strain	Peak Strain Rate (sec ⁻¹)	Normalized Peak Strain Rate (sec ⁻¹)
ε_r	-2.7 ± 0.4	-8.8 ± 1.3
ε_c	1.4 ± 0.2	$-6.4 \pm 0.9^*$
ε_l	1.2 ± 0.3	-7.7 ± 2.0
α_{c1}	$-55 \pm 12^\circ$	-7.7 ± 1.6

All values mean \pm SD.

* $P < .05$, in paired t -test vs. ε_r .

with Eq. (2) from reported values of E_{rr}), while Young reported a lower range 0.02–0.22. The mean values of ε_c and ε_l are very similar in the three studies: $\varepsilon_c = -0.21$, $\varepsilon_l = -0.16$ (this study), $\varepsilon_c = -0.23$, $\varepsilon_l = -0.18$,^[18] $\varepsilon_c = -0.23$, $\varepsilon_l = -0.19$.^[13] We did not find a significant variation in ε_r between the circumferential segments, which is probably related to the relatively large measurement error in radial strain.^[18,28]

The rc- and rl-shear strains showed much variance between subjects, as well as between various locations in the LV wall. At ES, both α_{rc} and α_{rl} were negative at the basal level, and positive at the apical level, in agreement with earlier publications.^[13,18] The relevance of these shear strains will be clarified when they are related to the fiber structures.^[29,30] Future applications of MR diffusion tensor imaging may provide in-vivo assessment of the fiber structures.^[31]

Diastolic Strain

We found a significant residual cl-shear strain at $t = \text{ES} + 270 \text{ msec}$ of $2.2 \pm 0.8^\circ$, equal 0.31 ± 0.11 in terms of normalized cl-shear. Thus, the average cl-shear at mid-diastole was 31% of the systolic shear. Similar results can be observed in Fig. 4 of Rademakers et al.^[7] concerning the mid-diastolic torsion in dogs. Figure 6A of Stuber et al.^[4] shows that they measured a slightly smaller mid-diastolic torsion of about 10–20% of the ES torsion. During diastole, the normal LV untwists before it fills,^[4,7] which is in agreement with our finding that the shear-cl recovers before the radial, circumferential, and longitudinal strains. It has been hypothesized that the untwisting during isovolumetric relaxation is a mechanism to enhance the pressure gradient between the left atrium and ventricle.^[7]

Limitations of This Study

In this study, we used the late-diastolic geometry of the LV to define the local cardiac coordinates for strain analysis. In principle, this should have been the geometry of the undeformed state (ED). In the tagged cine images, the first image after the R-wave does not have contrast between blood pool and heart wall. Consequently, the tagged images cannot provide a reliable estimate of the ED geometry. The technique of a blood saturation pulse used by Moore et al.^[18] does not provide a solution for diastolic strain analysis, because the saturation pulse must be applied in early diastole in order to be effective. The saturation pulse would interrupt equidistant data

acquisition in diastole. The late-diastolic geometry (approx. 750 msec after ED) used in this paper provides a reasonable estimate of the ED coordinate system when the shape of the LV is not drastically altered during contraction of the left atrium.

Our choice of 270 msec after ES as the point to end the analysis is somewhat arbitrary. However, data of individual subjects showed that rapid filling was sufficiently covered even for subjects with quiet heart rate (<60 bpm). For patients with slow LV filling, the rapid filling phase may not be completed within 270 msec. In these cases, impaired filling will be evident from the pattern in the first 270 msec. In addition, improvement in temporal resolution (30 msec in this study) may reveal other important information regarding early diastolic events, as well as provide more reliable estimates of the peak strain rate.

CONCLUSION

In this paper, we have presented the normal values for ES 3D strain and for the temporal evolution of 3D strain during diastole in the LV heart wall. We have shown that the diastolic strain can be assessed with MR-tagging using a time resolution of 30 msec. Compared to systolic tagging, diastolic tagging is more difficult due to tag line fading.

The measured diastolic strain evolution showed that the cl-shear strain, associated with LV torsion, decreased before the magnitude of the axial strains decreased, which is consistent with the observation of LV untwisting before filling. Diastolic 3D strain analysis may allow differentiation between normal and abnormal diastolic wall mechanics, which offers the prospect of noninvasive early detection of regional diastolic dysfunction.

ABBREVIATIONS

LV	left ventricle
ES	end systole
ED	end diastole
LA	long axis
SA	short axis
EDV	end-diastolic volume
ESV	end-systolic volume
EF	ejection fraction
CO	cardiac output
PFR	peak filling rate

SYMBOLS

F	deformation gradient tensor
E	Lagrangian strain tensor
ϵ	axial strain
α	shear strain
r	radial
c	circumferential
l	longitudinal
ϵ_r	radial strain
α_{cl}	circumferential–longitudinal shear strain
ϵ_{nor}	axial strain normalized to ES value
α_{nor}	shear strain normalized to ES value

REFERENCES

1. Lenihan, D.J.; Gerson, M.C.; Hoit, B.D.; Walsh, R.A. Mechanisms, Diagnosis, and Treatment of Diastolic Heart Failure. *Am. Heart J.* **1995**, *130*, 153–166.
2. Mandinov, L.; Eberli, F.R.; Seiler, C.; Hess, O.M. Diastolic Heart Failure. *Cardiovasc. Res.* **2000**, *45*, 813–825.
3. De Simone, G.; Greco, R.; Mureddu, G.; Romano, C.; Guida, R.; Celentano, A.; Contaldo, F. Relation of Left Ventricular Diastolic Properties to Systolic Function in Arterial Hypertension. *Circulation* **2000**, *101*, 152–157.
4. Stuber, M.; Scheidegger, M.B.; Fischer, S.E.; Nagel, E.; Steinemann, F.; Hess, O.M.; Boesiger, P. Alterations in the Local Myocardial Motion Pattern in Patients Suffering from Pressure Overload Due to Aortic Stenosis. *Circulation* **1999**, *100*, 361–368.
5. Bruch, C.; Schermund, A.; Bartel, T.; Schaar, J.; Erbel, R. Tissue Doppler Imaging (TDI) for On-Line Detection of Regional Early Diastolic Ventricular Asynchrony in Patients with Coronary Artery Disease. *Int. J. Card. Imaging* **1999**, *15*, 379–390.
6. Poulsen, S.H.; Jensen, S.E.; Egstrup, K. Longitudinal Changes and Prognostic Implications of Left Ventricular Diastolic Function in First Acute Myocardial Infarction. *Am. Heart J.* **1999**, *137*, 910–918.
7. Rademakers, F.E.; Buchalter, M.B.; Rogers, W.J.; Zerhouni, E.A.; Weisfeldt, M.L.; Weiss, J.L.; Shapiro, E.P. Dissociation Between Left Ventricular Untwisting and Filling. Accentuation by Catecholamines. *Circulation* **1992**, *85*, 1572–1581.
8. Nagel, E.; Stuber, M.; Burkhard, B.; Fischer, S.E.; Scheidegger, M.B.; Boesiger, P.; Hess, O.M. Cardiac Rotation and Relaxation in Patients with Aortic Valve Stenosis. *Eur. Heart J.* **2000**, *21*, 582–589.
9. Dong, S.J.; Hees, P.S.; Huang, W.M.; Buffer, S.A.J.; Weiss, J.L.; Shapiro, E.P. Independent Effects of Preload, Afterload, and Contractility on Left Ventricular Torsion. *Am. J. Physiol.* **1999**, *277*, H1053–H1060.
10. Zerhouni, E.A.; Parish, D.M.; Rogers, W.J.; Yang, A.; Shapiro, E.P. Human Heart: Tagging with MR Imaging—A Method for Noninvasive Assessment of Myocardial Motion. *Radiology* **1988**, *169*, 59–63.
11. Axel, L.; Dougherty, L. MR Imaging of Motion with Spatial Modulation of Magnetization. *Radiology* **1989**, *171*, 841–845.
12. Götte, M.J.W.; Van Rossum, A.C.; Marcus, J.T.; Kuijjer, J.P.A.; Axel, L.; Visser, C.A. Recognition of Infarct Localization by Specific Changes in Intramural Myocardial Mechanics. *Am. Heart J.* **1999**, *138*, 1038–1045.
13. Young, A.A.; Kramer, C.M.; Ferrari, V.A.; Axel, L.; Reichek, N. Three-Dimensional Left Ventricular Deformation in Hypertrophic Cardiomyopathy. *Circulation* **1994**, *90*, 854–867.
14. Lima, J.A.; Ferrari, V.A.; Reichek, N.; Kramer, C.M.; Palmon, L.; Llaneras, M.R.; Tallant, B.; Young, A.A.; Axel, L. Segmental Motion and Deformation of Transmurally Infarcted Myocardium in Acute Postinfarct Period. *Am. J. Physiol.* **1995**, *268*, H1304–H1312.
15. Azhari, H.; Weiss, J.L.; Rogers, W.J.; Siu, C.O.; Shapiro, E.P. A Noninvasive Comparative Study of Myocardial Strains in Ischemic Canine Hearts Using Tagged MRI in 3-D. *Am. J. Physiol.* **1995**, *268*, H1918–H1926.
16. Croisille, P.; Moore, C.C.; Judd, R.M.; Lima, J.A.; Arai, M.; McVeigh, E.R.; Becker, L.C.; Zerhouni, E.A. Differentiation of Viable and Nonviable Myocardium by the Use of Three-Dimensional Tagged MRI in 2-Day-Old Reperfused Canine Infarcts. *Circulation* **1999**, *99*, 284–291.
17. Prinzen, F.W.; Hunter, W.C.; Wyman, B.T.; McVeigh, E.R. Mapping of Regional Myocardial Strain and Work During Ventricular Pacing: Experimental Study Using Magnetic Resonance Imaging Tagging. *J. Am. Coll. Cardiol.* **1999**, *33*, 1735–1742.
18. Moore, C.C.; Lugo-Olivieri, C.H.; McVeigh, E.R.; Zerhouni, E.A. Three-Dimensional Systolic Strain Patterns in the Normal Human Left Ventricle: Characterization with Tagged MR Imaging. *Radiology* **2000**, *214*, 453–466.
19. Rademakers, F.E.; Herregods, M.C.; Marchal, G.; Bogaert, J. Contradictory Effect of Aging on Left Ventricular Untwisting and Filling [Abstract]. *Circulation* **1996**, *94*, I-65.
20. Buchalter, M.B.; Weiss, J.L.; Rogers, W.J.; Zerhouni, E.A.; Weisfeldt, M.L.; Beyar, R.; Shapiro, E.P. Noninvasive Quantification of Left Ventricular Rotational Deformation in Normal Humans Using Magnetic Resonance Imaging Myocardial Tagging. *Circulation* **1990**, *81*, 1236–1244.
21. Kuijjer, J.P.A.; Marcus, J.T.; Götte, M.J.W.; Van Rossum, A.C.; Heethaar, R.M. Three-Dimensional Myocardial Strain Analysis Based on Short- and Long-Axis Magnetic

- Resonance Tagged Images Using a 1D Displacement Field. *Magn. Reson. Imaging* **2000**, *18*, 553–564.
22. Marcus, J.T.; De Waal, L.K.; Gotte, M.J.W.; Van der Geest, R.J.; Heethaar, R.M.; Van Rossum, A.C. MRI-Derived Left Ventricular Function Parameters and Mass in Healthy Young Adults: Relation with Gender and Body Size. *Int. J. Card. Imaging* **1999**, *15*, 411–419.
 23. Doyle, M.; Scheidegger, M.B.; De Graaf, R.G.; Vermeulen, J.; Pohost, G.M. Coronary Artery Imaging in Multiple 1-sec Breath Holds. *Magn. Reson. Imaging* **1993**, *11*, 3–6.
 24. Kraitchman, D.L.; Young, A.A.; Chang, C.N.; Axel, L. Semi-automatic Tracking of Myocardial Motion in MR Tagged Images. *IEEE Trans. Med. Imaging* **1995**, *14*, 422–433.
 25. Young, A.A.; Axel, L. Three-Dimensional Motion and Deformation of the Heart Wall: Estimation with Spatial Modulation of Magnetization—A Model-Based Approach. *Radiology* **1992**, *185*, 241–247.
 26. Axel, L.; Gonçalves, R.C.; Bloomgarden, D.C. Regional Heart Wall Motion: Two-Dimensional Analysis and Functional Imaging with MR Imaging. *Radiology* **1992**, *183*, 745–750.
 27. Fung, Y.C. *A First Course in Continuum Mechanics: For Physical and Biological Scientists and Engineers*; Prentice-Hall: Englewood Cliffs, 1994.
 28. Young, A.A.; Axel, L.; Dougherty, L.; Bogen, D.K.; Parenteau, C.S. Validation of Tagging with MR Imaging to Estimate Material Deformation. *Radiology* **1993**, *188*, 101–108.
 29. Legrice, I.J.; Takayama, Y.; Covell, J.W. Transverse Shear Along Myocardial Cleavage Planes Provides a Mechanism for Normal Systolic Wall Thickening. *Circ. Res.* **1995**, *77*, 182–193.
 30. Costa, K.D.; Takayama, Y.; McCulloch, A.D.; Covell, J.W. Laminar Fiber Architecture and Three-Dimensional Systolic Mechanics in Canine Ventricular Myocardium. *Am. J. Physiol.* **1999**, *276*, H595–H607.
 31. Reese, T.G.; Weisskoff, R.M.; Smith, R.N.; Rosen, B.R.; Dinsmore, R.E.; Wedeen, V.J. Imaging Myocardial Fiber Architecture In Vivo with Magnetic Resonance. *Magn. Reson. Med.* **1995**, *34*, 786–791.

Received November 18, 2001

Accepted February 1, 2002